RESEARCH ARTICLE

**ADVANCED
NANOBIOMED
RESEARCH**
Open Access

www.advnanobiomedres.com

Graphene Nanoflake Antibody Conjugates for Multimodal Imaging of Tumors

Jennifer Lamb, Joris Šimaitis, Siriney O. Halukeerthi, Christoph G. Salzmann, and Jason P. Holland*

Graphene-based materials are promising scaffolds for use in the design of tailored-made nanomedicines. Herein, the synthesis and characterization of a series of multifunctional carboxylated graphene nanoflakes (GNFs) conjugated to monoclonal antibodies (mAbs) for tumor-specific binding and modulation of pharmacokinetics is presented. GNF–mAb constructs are coupled to a fluorophore (4,4-difluoro-4-bora-3a,4a-diaza-s-indacene [BODIPY]) for applications in optical imaging, a paramagnetic Gd^{3+} complex, $[GdDOTAGA(H_2O)]^-$, and the hexadentate chelate desferrioxamine B (DFO) for radiolabeling with $^{89}Zr^{4+}$ ($t_{1/2} = 78.41$ h) ions and applications in dual-modality positron emission tomography/magnetic resonance imaging (PET/MRI). Experimental properties of [^{89}Zr]GdDOTAGA–ZrDFO–GNF–trastuzumab are tested in extensive chemical, spectroscopic, radiochemical, and cellular assays in vitro, and assessment of the pharmacokinetics by PET imaging in mice bearing a human ovarian cancer model illustrates the potential of using GNF–mAbs to develop multifunctional PET/MRI probes.

1. Introduction

The versatile properties of graphene materials such as carbon nanotubes, graphene oxide (GO), and reduced GO (rGO) nanoparticles have been harnessed to produce multimodality agents for diagnostic imaging and targeted drug delivery in cancers.[1–19] In an early example of using graphene-based materials in nanomedicine, McDevitt et al. conjugated rituximab to carbon nanotubes by using a maleimide coupling to the cysteine residues.[3] Subsequently, Ruggiero et al. investigated the properties of radiolabeled single-walled carbon nanotubes (SWCNTs) functionalized with the E4G10 mAb for targeting the monomeric vascular endothelial-cadherin epitope present on many types of pro-angiogenic tumors.[9] A ^{89}Zr-radiolabeled SWCNT–mAb showed promise for diagnostic positron emission tomography (PET) whereas a parallel construct bearing an α-particle emitter ^{225}AcDOTA complex was used for molecularly targeted radioimmunotherapy (RIT). Recently, Li et al. produced antibody-modified rGO films by functionalization of the pyrene carboxylic acid groups using 1-ethyl-3-(3-dimethylaminopropyl)carbodiimide/sulfo-N-hydroxysuccinimide (NHS) activation and amide bond formation with lysine residues on the protein.[2] Incorporation of monoclonal antibodies (mAbs) onto the rGO scaffold gave reagents that displayed extremely high sensitivity for the detection of circulating tumor cells. The therapeutic properties of metal-filled multiwalled carbon nanotubes (MWCNTs),[20] and GO nanocomposites functionalized with quantum dots,[21] have also been investigated as materials for photothermal therapy. Yang et al. loaded nanographene oxide with iron oxide nanoparticles as well as the chemotherapeutic drug epirubicin producing a theranostic construct that can be guided by magnetic targeting and tracked by magnetic resonance imaging (MRI).[22] Despite recent progress, the complex architecture of many nanomedicines often leads to suboptimal pharmacokinetics in vivo whereby the particles exhibit reduced metabolic stability, limited tumor uptake, and short blood-pool circulation times coincident with rapid clearance by either the reticuloendothelial system or renal excretion pathways.[23,24] Much work is required to understand the in vivo behavior, intracellular transport, metabolism, and excretion of graphene-based nanomaterials.[25–28]

Dr. J. Lamb, Prof. J. P. Holland
Department of Chemistry
University of Zurich
Winterthurerstrasse 190, Zurich CH-8057, Switzerland
E-mail: jason.holland@chem.uzh.ch

J. Šimaitis, S. O. Halukeerthi, Prof. C. G. Salzmann
Department of Chemistry
University College London
20 Gordon Street, London WC1H 0AJ, UK

2. Results and Discussion

Graphene nanoflakes (GNFs) consist of a single graphene sheet with a pristine aromatic system and an edge that is terminated with carboxylic acid groups.[29,30] GNF particles range in size with current technology providing reliable access to flakes with an average diameter of 30 ± 9 nm. Atomic force microscopy (AFM), X-ray photoelectron spectroscopy, and Fourier-transform infrared (FT–IR) data of pristine GNFs are shown in **Figure 1**. The carboxylated edge of GNFs is accessible for functionalization

**ADVANCED
SCIENCE NEWS**
www.advancedsciencenews.com

**ADVANCED
NANOBIOMED
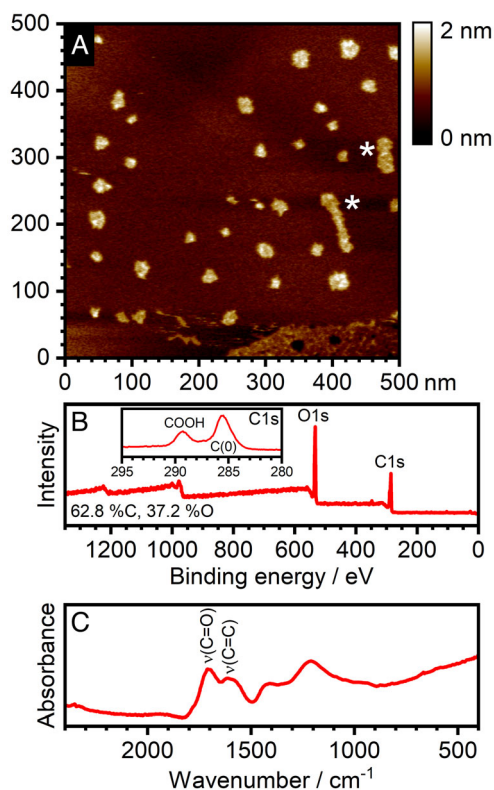RESEARCH**
Open Access
www.advnanobiomedres.com

Figure 1. Structure and chemical composition of carboxylated GNFs. A) AFM image of GNFs spin coated onto a pyrolytic graphite substrate from aqueous dispersion. The two flakes marked with asterisks were dragged across the surface by the ATM tip. B) X-ray photoelectron spectroscopy survey spectrum illustrating the purity of the GNF sample containing only carbon and oxygen. The C1s region in the inset indicates the presence of graphitic carbon and carboxylic acid groups. C) FT–IR spectrum of GNFs with a $\nu(C = O)$ stretching mode of COOH at $\approx 1707\,cm^{-1}$.

with drug molecules but as with other graphene-based nanomedicines, PET imaging in mice revealed rapid (essentially first pass) filtration through the kidneys and excretion in the urine.[12] To modulate the pharmacokinetics, we hypothesized that functionalizing GNFs with cancer-specific mAbs would increase circulation times and enhance tumor uptake. Here, we present the synthesis and characterization of different GNF–mAb constructs for multimodality imaging of cancer. An illustration of the chemical structure of a small GNF and a depiction of the different constructs synthesized and tested is shown in **Figure 2**.

To facilitate the analysis and optimization of the conjugation chemistry between the GNF and the mAb, experiments began by coupling the 4,4-difluoro-4-bora-3a,4a-diaza-_s_-indacene (BODIPY) scaffold to GNFs (**Figure 3**; Scheme S1 and S2, Figure S1 and S2, Supporting Information). BODIPY compound 2, featuring a free aniline, was synthesized in 13% overall yield and characterized by NMR spectroscopy. Coupling of BODIPY (2) to GNFs produced the optically active BODIPY–GNF construct, which was characterized by electronic absorption spectroscopy (UV/vis), fluorescence emission spectroscopy, thin-layer chromatography (TLC; Figure S3, Supporting Information), and size-exclusion chromatography (SEC) coupled to high-performance liquid chromatography

(SEC–HPLC; Figure 3B, red trace). Electronic absorption and fluorescence emission spectroscopy confirmed the successful conjugation of BODIPY to the GNF where both the absorption and emission profiles matched that of the free BODIPY dye ($\lambda_{abs,max} = 498\,nm$, $\lambda_{em,max} = 510\,nm$) indicating that the fluorophore remained electronically decoupled from the aromatic system of the GNF.

Next, functionalization of BODIPY–GNF with tumor-specific mAbs was accomplished by a two-step process involving activation of the carboxylated edge with NHS followed by amide bond formation with surface-exposed lysine residues (Scheme S3, Supporting Information). Separate reactions with trastuzumab (a humanized IgG_1 targeting human epidermal growth factor receptor 2, HER2/_neu_) and onartuzumab (a monovalent one-armed engineered antibody that binds to an extracellular epitope of the human hepatocyte growth factor receptor, c-MET) produced BODIPY–GNF–trastuzumab and BODIPY–GNF–onartuzumab, respectively. For the BODIPY–GNF–trastuzumab construct, SEC–HPLC (Figure 3B) monitored at different wavelengths confirmed that the BODIPY–GNF was covalently conjugated to the protein as evidenced by coelution of peaks in the BODIPY (490 nm; blue trace) and the protein (280 nm; green trace) channels. The resolution of SEC–HPLC is insufficient to provide a definitive stoichiometric analysis, but notably, the major peak eluted with a similar retention time to that of free trastuzumab (Figure 3B; black trace, $\approx 18.1\,min$) suggesting that a majority of the BODIPY–GNF–trastuzumab sample contained $\approx 1\,mAb$ per GNF. In reactions that used higher amounts of initial protein, products contained an increased proportion of BODIPY–GNF–trastuzumab whereby the GNF was functionalized with 2 or more mAbs (Figure S4, Supporting Information).

Cellular binding assays were used to assess the specific tumor binding and immunoreactivity of the BODIPY–GNF–trastuzumab construct (Figure 3C,D). SK-OV-3 ovarian cancer cells are well-known to overexpress the HER2/_neu_ antigen. Fluorescence-assisted cell sorting (FACS) revealed a statistically significant increase in fluorescence intensity (≈ 2.7-fold) in samples that are treated with BODIPY–GNF–mAb compared with the vehicle-treated controls (P value < 0.01). Two further controls were also performed to confirm the binding specificity. First, incubation of cells with the nontargeted BODIPY–GNF (control) construct gave a fluorescence intensity identical to that of the vehicle control (≈ 2.2-fold decrease, P value < 0.05 compared with BODIPY–GNF–trastuzumab). Second, blocking experiments involving preincubation of the cells with an excess of nonlabeled trastuzumab followed by the addition of BODIPY–GNF–trastuzumab also reduced cell-associated fluorescence intensity to baseline levels (≈ 2.2-fold decrease, P value < 0.05 compared with BODIP–GNF–trastuzumab alone). Equivalent results using SEC–HPLC and FACS studies with MKN-45 human gastrocarcinoma cells (c-MET positive) were obtained for the BODIPY–GNF–onartuzumab construct (Figure S5, Supporting Information). Encouragingly, experiments with these two BODIPY–GNF–mAb constructs confirmed that functionalization of GNFs with diagnostic imaging agents and mAbs is feasible, resulting in nanoparticles that retain tumor-specific immunoreactivity. These BODIPY–GNF–mAbs are also promising tools for the optical detection and quantification of cancer biomarker expression in vitro and in vivo.
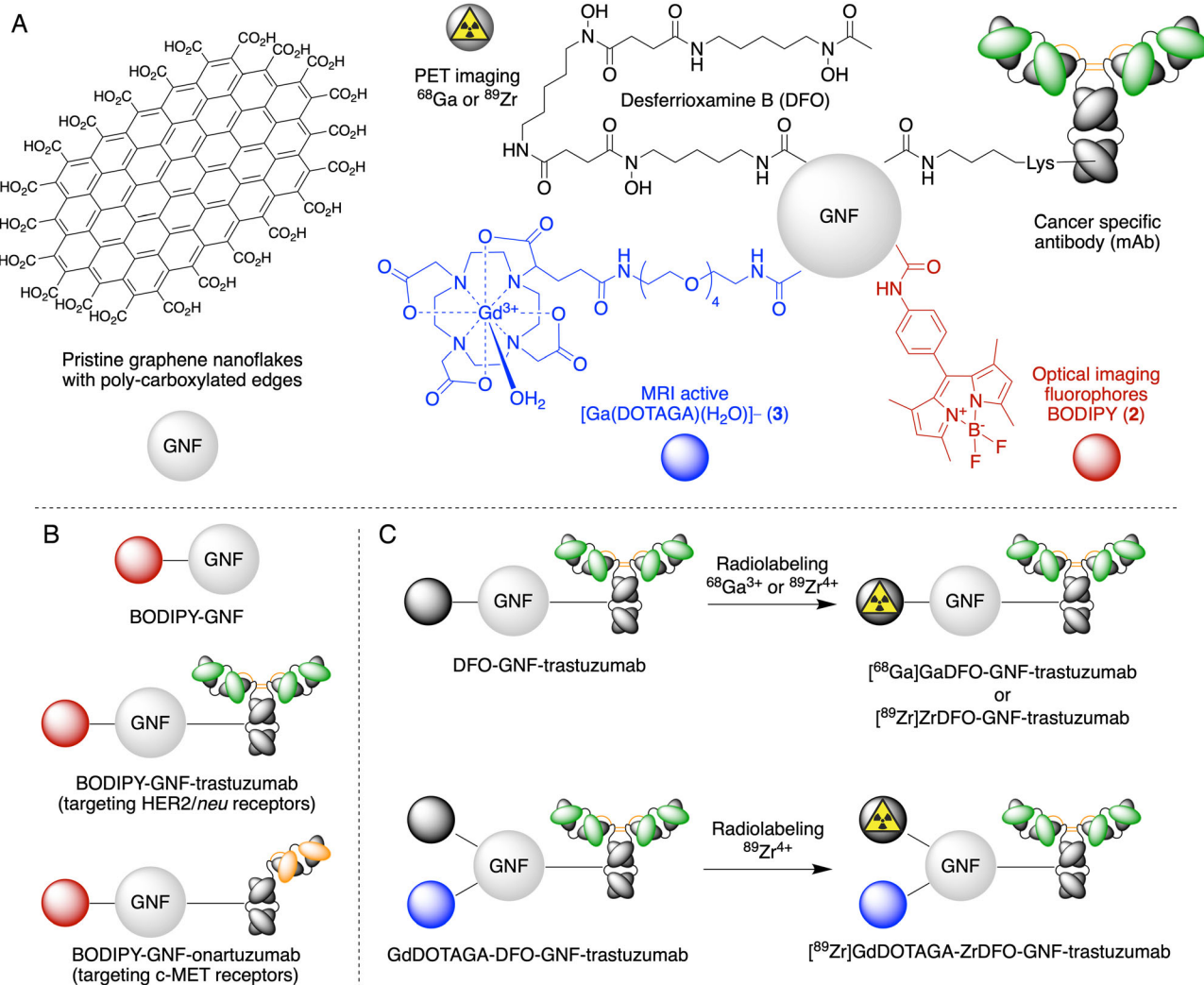
Figure 2. A) Schematic representation of a small GNF and the covalent conjugation of the optically active BODIPY fluorophore, the MRI active [GaDOTAGA(H$_2$O)]$^-$ complex, the DFO ligand for radiolabeling with ^{68}Ga^{3+} or ^{89}Zr^{4+} ions, and functionalization with a cancer biomarker-specific mAb for tumor targeting. Bottom panels show schematic structures of, B) the optically active and C) the PET/MRI active GNF constructs synthesized.

The reduced size of the monovalent engineered onartuzumab protein (99 kDa) compared with the bivalent full-sized trastuzumab (≈150 kDa) led to more challenging purification by manual size-exclusion methods. Therefore, further studies on the development of a multimodal PET/MRI construct used trastuzumab. Conjugation of the metal binding chelate desferrioxamine B (DFO) to GNFs gave the DFO–GNF construct.[12] This material was then functionalized with trastuzumab to give DFO–GNF–trastuzumab (Scheme S4, Supporting Information) which was characterized by SEC–HPLC (Figure S6, Supporting Information). ^{89}Zr-radiolabeling and purification by sized-exclusion methods produced [^{89}Zr]ZrDFO–GNF–trastuzumab with a decay-corrected radiochemical yield (RCY) of 28% and a radiochemical purity (RCP) of 82%. The [^{89}Zr]ZrDFO–GNF–trastuzumab radiotracer was characterized by radioactive instant TLC (radio-iTLC), manual SEC with PD-10 columns, and SEC–HPLC (Figure S7, Supporting Information). Control experiments found no specific binding of

^{89}Zr^{4+} ions to pristine GNF. Collectively, these data confirm the presence of DFO on the GNF. Cellular saturation binding (Lindmo) assays were used to measure the specific binding and immunoreactive fraction (Figure S8, Supporting Information). [^{89}Zr]ZrDFO–GNF–trastuzumab displayed specific binding to SK-OV-3 cells in vitro with an immunoreactive fraction of $58.0 \pm 2.3\%$. Although the [^{89}Zr]ZrDFO–GNF–trastuzumab is a potential PET radiotracer, the value of functionalizing mAbs with GNF constructs lies in the increased loading capacity which offers the possibility of attaching different components to access multi-modality imaging agents. For a typical radiolabeled mAb, a ligand-to-protein ratio of 1 is ideal to minimize the loss of biochemical integrity. However, with approximately seven orders of magnitude difference in the administered concentration of a PET radiotracer and an MRI contrast agent, increased ligand stoichiometry is required.[31,32] Multifunctionalized GNF–mAbs offer a potential solution to bridge the sensitivity gap between PET and MRI.
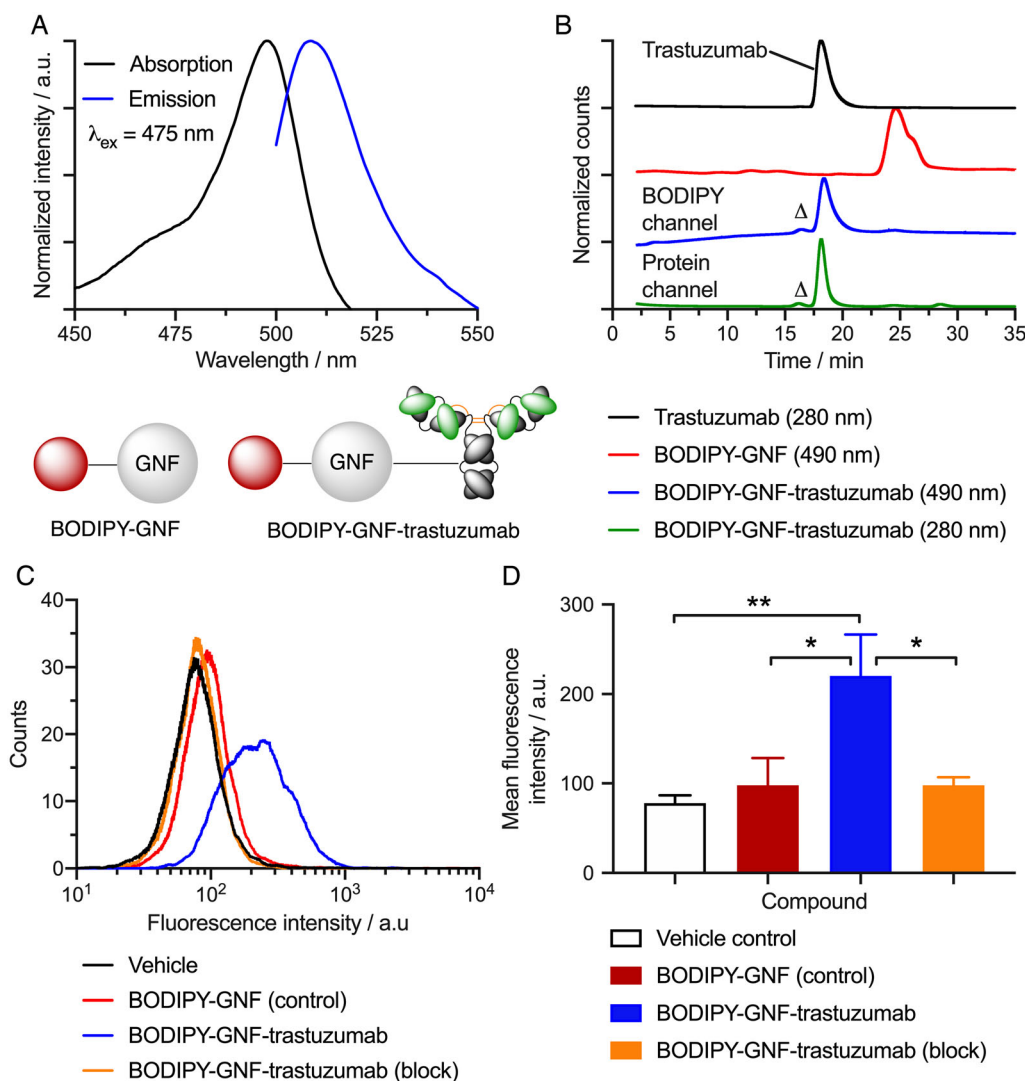
Figure 3. Characterization of the BODIPY–GNF–trastuzumab construct. A) Optical absorption (black) and fluorescence emission profiles of BODIPY–GNF (control) confirming the successful conjugation of BODIPY to the GNF via amide bond formation. B) Size-exclusion HPLC chromatograms showing the elution time of native trastuzumab (black trace), BODIPY–GNF control particles (red trace), and two traces of the BODIPY–GNF–trastuzumab construct showing coelution of the BODIPY channel (490 nm; blue trace) with the protein channel (280 nm, green trace) and confirming the purity via the absence of a peak for the protein-free BODIPY–GNFs. Note: Δ indicates the elution of high molecular weight GNF aggregates that contain 2 or more mAbs per GNF. C) One-dimensional FACS data showing the measured counts versus fluorescence intensity (a.u.). D) Plot of the mean fluorescence intensity (a.u.) from the FACS data for SK-OV-3 cells treated with vehicle control (white bar), the BODIPY–GNF control (red bar), BODIPY–GNF–trastuzumab (blue bar), and a blocking control involving pretreatment with a 333-fold excess of trastuzumab (orange bar). Note: ** P value < 0.01, * P value < 0.05.

In the next step, the MRI active GdDOTAGA–PEG$_4$–NH$_2$ complex (3) was synthesized and characterized prior to coupling to the GNF (Scheme S5 and Figure S9, Supporting Information). Synthesis of the radiolabeling precursors GdDOTAGA–DFO–GNF, and GdDOTAGA–DFO–GNF–trastuzumab was accomplished by using the amide conjugation methods established in the BODIPY–GNF work (Scheme S6, Supporting Information). GdDOTAGA–DFO–GNF was characterized by TLC (Figure S10, Supporting Information) and radiolabeling studies with either ^{68}Ga^{3+} ($t_{1/2} = 67.71$ min) or ^{89}Zr^{4+} ions confirmed the presence of DFO. Accurate knowledge of the molar activity of the $[^{68}$Ga]Ga(H$_2$O)$_6$]Cl$_3$(aq.) stock solution

allowed experimental measurement of the DFO content which was found to be 13.4 ± 1.8 nmol DFO per mg of GNF ($n = 2$; Figure S11, Supporting Information). ^{89}Zr-radiolabeling gave $[^{89}$Zr]GdDOTAGA–ZrDFO–GNF which was characterized by radio-iTLC and radioactive SEC–HPLC and obtained with a decay-corrected RCY of 97% and a RCP of 98% (Figure S12, Supporting Information). T_1 measurements using NMR confirmed that presence of the paramagnetic Gd^{3+} ion on the GdDOTAGA–DFO–GNF construct with a calculated r_1 relaxivity of 0.88 ± 0.03 mL mg^{-1} s^{-1} (by GNF mass) (Figure S13, Supporting Information). From the measured T_1-relaxation times at a given concentration of GNF, it was estimated that

**ADVANCED
SCIENCE NEWS**

www.advancedsciencenews.com

**ADVANCED
NANOBIOMED
RESEARCH**
Open Access

www.advnanobiomedres.com

the GdDOTAGA–DFO–GNF contains 45.0 ± 4.3 nmol of GdDOTAGA–PEG$_4$–NH$_2$ per mg of GNF. Therefore, the GdDOTAGA to DFO ratio was $\approx$3.4-to-1 confirming that multifunctional PET/MRI agents can be made using the GNF scaffold.

Conjugation of GdDOTAGA–DFO–GNF to trastuzumab and ^{89}Zr-radiolabeling of the GdDOTAGA–DFO–GNF–trastuzumab construct was accomplished by the established routes (Scheme S6, Supporting Information). Addition of the mAb to form GdDOTAGA–DFO–GNF–trastuzumab gave a measured r_1 relaxivity of 0.077 ± 0.001 mL mg^{-1} s^{-1} by protein mass. The radiolabeled construct [^{89}Zr]GdDOTAGA–ZrDFO–GNF–trastuzumab was characterized by radio-iTLC, analytical size-exclusion (PD-10) chromatography, and by SEC–HPLC (**Figure 4**). To ensure complete radiolabeling of all available DFO ligands, an excess of the ^{89}Zr stock solution was used, and therefore, the overall RCY of the isolated product was low ($9.4 \pm 4.5\%$; $n = 3$) with a final RCP of $91.4 \pm 1.4\%$ ($n = 3$; determined by radioactive PD10 analysis). Stability studies in vitro confirmed that [^{89}Zr]GdDOTAGA–ZrDFO–GNF–trastuzumab remained intact with respect to changes in RCP when incubated with excess diethylenetriaminepentaacetic acid (DTPA; Figure S14, Supporting Information). Cellular saturation binding (Lindmo) assays confirmed that [^{89}Zr]GdDOTAGA–ZrDFO–GNF–trastuzumab remained specific toward HER2/*neu* with an immunoreactive fraction of $62 \pm 11\%$ (Figure 4D,E).

The pharmacokinetics and tumor-specific uptake of [^{89}Zr]GdDOTAGA–ZrDFO–GNF–trastuzumab was measured by PET imaging and biodistribution studies in mice bearing subcutaneous SK-OV-3 xenografts (**Figure 5**, and S15, Supporting Information). Temporal PET images recorded from 1 to 90 h postintravenous (i.v.) administration of [^{89}Zr]GdDOTAGA–ZrDFO–GNF–trastuzumab show accumulation of the radioactivity in tumors for the normal group of animal ($n = 4$). In a control (blocking) group ($n = 4$), coadministration of a 15.4-fold excess dose of trastuzumab (by protein mass) demonstrated the specificity of tumor uptake (Figure S16, Supporting Information). PET data were quantified by volume-of-interest (VOI) analysis, and time-activity curves (TACs) showing the radiotracer pharmacokinetics in selected organs are given in Figure S15B, Supporting Information. Analysis of the TACs drawn over the left ventricle of heart which reflect circulating blood pool activity confirmed that no mass-dependent differences were observed between the normal and blocking groups (Figure S15C, Supporting Information). In contrast to GNFs functionalized with a small-molecule drugs,[12] the [^{89}Zr]GdDOTAGA–ZrDFO–GNF–trastuzumab remained in circulation with an effective blood pool half-life, $t_{1/2}$(blood), of 7.05 ± 1.03 h ($n = 4$). Additional control images using [^{89}Zr]GdDOTAGA–ZrDFO–GNF indicated that the extended circulation time was the result of successful protein conjugation to the GNF (Figure S12C, Supporting Information). After recording the final image at 90 h, mice were euthanized and biodistribution data were recorded (Figure 5B;
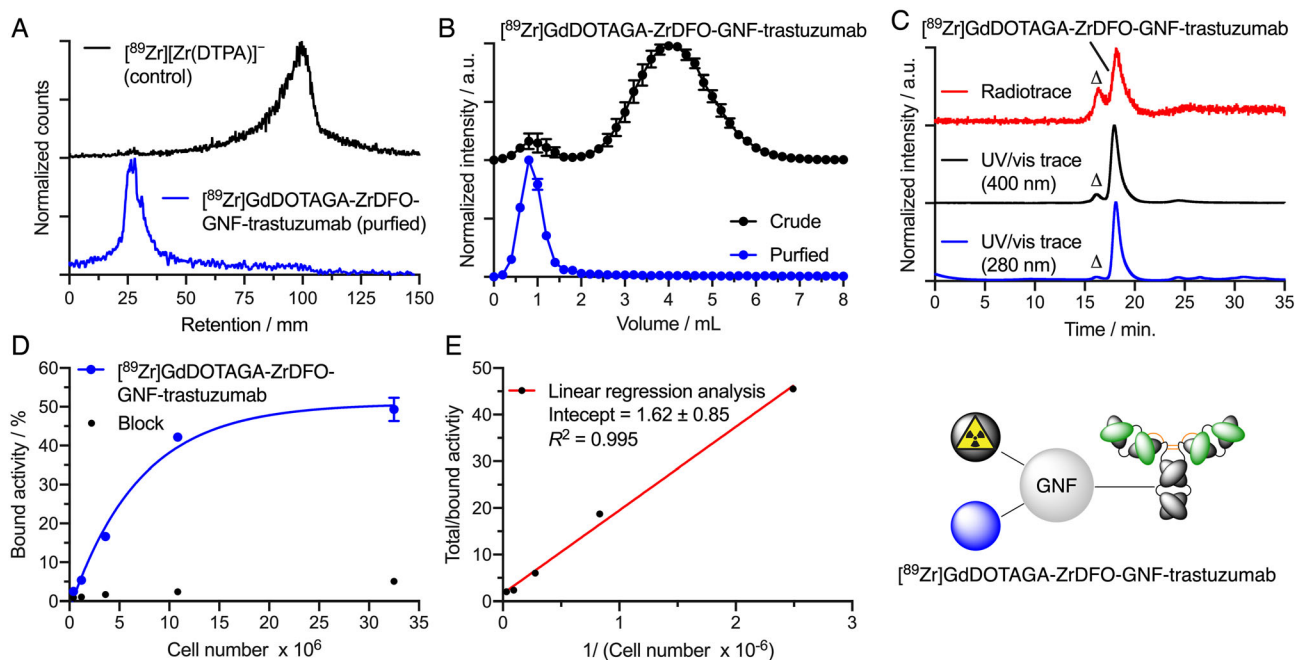

Figure 4. ^{89}Zr-radiolabeling and cellular binding with [^{89}Zr]GdDOTAGA–ZrDFO–GNF–trastuzumab. A) Radio-iTLC chromatograms showing the retention of the purified [^{89}Zr]GdDOTAGA–ZrDFO–GNF–trastuzumab product at the baseline ($R_f = 0.0$; blue trace) versus "free" [^{89}Zr][Zr(C$_2$O$_4$)$_4$]$^{4-}$ control ($R_f = 0.9$–1.0; black trace). B) Manual PD-10-SEC chromatograms for the crude (black) and purified (blue) products. C) SEC–HPLC chromatograms of the purified product showing the radioactive trace (red) and the GNF component (400 nm, black) and the protein component (280 nm, blue). Note: Δ indicates the elution of high molecular weight aggregate GNF species that contain 2 or more mAbs per GNF. D) Cellular saturation binding curve showing the binding of [^{89}Zr]GdDOTAGA–ZrDFO–GNF–trastuzumab to SK-OV-3 (HER2/*neu* positive) cells (blue) versus a blocking study with a 1000-fold excess of trastuzumab (black dots). E) Lindmo transformation for estimating the immunoreactive fraction of the purified radiotracer.
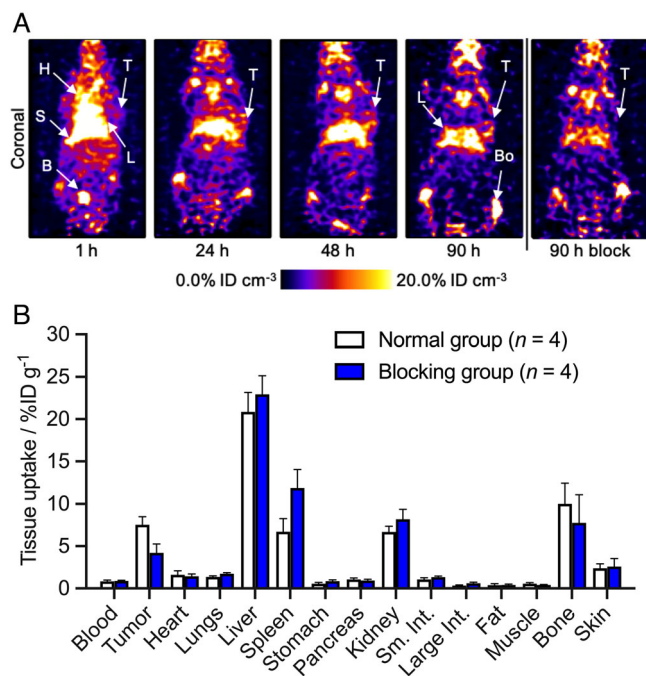
Figure 5. Pharmacokinetics, biodistribution, and tumor-specific uptake of [89Zr]GdDOTAGA–ZrDFO–GNF–trastuzumab in female athymic nude mice bearing subcutaneous SK-OV-3 tumors on the right flank ($n = 4$ mice/group). A) Temporal coronal PET images taken through the tumor center showing radiotracer uptake and distribution up to 90 h postadministration. Further images are shown in Figure S15 and S16, Supporting Information. H = heart, S = spleen, B = bladder, T = tumor, Bo = bone. B) Ex vivo biodistribution data showing the accumulated radioactivity in different tissues/organs after the final imaging time point (90 h postadministration).

Table S1 and S2, and Figure S17, Supporting Information). Tumor-associated radioactivity in the normal group reached $7.53 \pm 0.83\%$ID g^{-1} whereas in the blocking group, an $\approx 45\%$ reduction in tumor uptake was observed ($4.21 \pm 0.74\%$ID g^{-1}). Notably, the tumor uptake in the normal group was significantly higher than the blood pool activity ($0.84 \pm 0.12\%$ID g^{-1}). Activity was also found in the liver ($20.87 \pm 1.98\%$ID g^{-1}), kidney ($6.68 \pm 0.60\%$ID g^{-1}), and bone ($10.02 \pm 1.73\%$ID g^{-1}). Activity in the liver was not observed in images of the control construct [89Zr]GdDOTAGA–ZrDFO–GNF. Bone uptake is high but comparable to that observed for classic 89Zr-DFO-labeled mAbs and is potentially associated with metabolism of the ZrDFO complex in the liver or tumor.[33–35] Finally, whole-body excretion measurements gave an effective half-life of [89Zr]GdDOTAGA–ZrDFO–GNF–trastuzumab of ≈ 31.5 h for the normal group, ≈ 29.9 h for the blocking group, and only ≈ 0.4 h for the [89Zr]GdDOTAGA–ZrDFO–GNF control (Figure S15E, Supporting Information). Collectively, these data provide compelling evidence of successful GNF functionalization with trastuzumab. We note that the exact mechanisms of graphene-based nanoparticle excretion and metabolism have not been studied in detail. Future work on the development of GNFs as tumor-specific drug-delivery vectors will be needed to investigate the phenomenon of in vivo metabolism and renal excretion in detail.

3. Conclusion

In conclusion, the experimental data acquired by using chemical, radiochemical, optical spectroscopy, cellular binding assays, and full pharmacokinetic analysis via PET imaging and biodistribution studies confirm that GNFs are a flexible platform for the future design of multimodality nanomedicines for optical imaging, PET/MRI, and tumor-specific drug delivery.

4. Experimental Section

General information on the methods and materials, as well as further experimental details on the synthesis, radiochemistry, cellular assays, small-animal PET imaging, and biological studies on animals are presented in the Supporting Information.

Radioactivity: All instruments for measuring radioactivity were calibrated and maintained in accordance with previously reported routine quality control procedures.[36] [89Zr][Zr(C$_2$O$_4$)$_4$]$^{4-}$(aq.) was obtained as a solution in ≈ 1.0 M oxalic acid from PerkinElmer (Boston, MA, manufactured by the BV Cyclotron VU, Amsterdam, The Netherlands) and was used without further purification. Radioactive reactions were monitored by using radio-iTLC. Glass-fiber iTLC plates impregnated with silica gel (iTLC-SG, Agilent Technologies) were developed in using DTPA (50 mM, pH7.4) and were analyzed on a radio-TLC detector (SCAN-RAM, LabLogic Systems Ltd, Sheffield, UK). Radiochemical conversion (RCC) was determined by integrating the data obtained by the radio-TLC plate reader and determining both the percentage of radiolabelled product ($R_f = 0.0$) and "free" 89Zr ($R_f = 1.0$; present in the analyses as either [89Zr]Zr(EDTA) or [89Zr][Zr(DTPA)]$^-$. Integration and data analysis were performed by using the software Laura version 5.0.4.29 (LabLogic).

[68Ga][Ga(H$_2$O)$_6$]Cl$_3$(aq.) was obtained from 68Ge/68Ga-generators (Eckert&Ziegler, Model IGG100 Gallium-68 Generator), eluted with 0.1 M HCl(aq.). The eluted 68Ga activity was trapped and purified by using a strong cation exchange column (Strata-XC, [SCX], Eckert&Ziegler). [68Ga][Ga(H$_2$O)$_6$]Cl$_3$(aq.) was eluted from the SCX cartridge by using a solution containing 0.13 M HCl(aq.) and ≈ 5 M NaCl(aq.) (SCX eluent). The generator gave molar activities in the range of 197 ± 4.82 MBq nmol^{-1}. For radiolabeling experiments, the 68Ga stock solution was typically added as the limiting reagent to an aqueous reaction mixture buffered with NaOAc (≈ 0.2 M, pH4.4). Radioactive reactions were monitored by using iTLC. Glass-fiber iTLC plates impregnated with silica gel (iTLC-SG, Agilent Technologies) were developed in citrate buffer (1.0 M, pH4.5) (>18.2 MΩ cm) and analyzed on a radio-TLC detector (SCAN-RAM, LabLogic Systems Ltd, Sheffield, UK). RCC was determined by integrating the data obtained by the radio-TLC plate reader and determining both the percentage of radiolabelled product ($R_f = 0.0$) and "free" 68Ga ($R_f = 1.0$). Integration and data analysis were performed by using the software Laura version 5.0.4.29 (LabLogic).

Appropriate background and decay corrections were applied as necessary. RCPs of labeled protein samples were determined by SEC using two different columns and techniques. The first technique used an automated size-exclusion column (Bio-Rad Laboratories, ENrich SEC 70, 10 ± 2 μm, 10 mm ID × 300 mm) connected to a UHPLC device (Hitachi ChromasterUltra Rs, VWR International, Leuven, Belgium) equipped with a UV/visible diode array detector (absorption measured at 220, 280, 400, and/or 490 nm) as well as a radioactivity detector (FlowStar^2 LB 514, Berthold Technologies, Zug, Switzerland). Isocratic elution with phosphate-buffered saline (PBS, pH7.4) was used. The second method used a manual procedure involving size-exclusion column chromatography using a PD-10 desalting column (Sephadex G-25 resin, 85–260 μm, 14.5 mm ID × 50 mm, >30 kDa, GE Healthcare). For analytical procedures, PD-10 columns were eluted with sterile PBS. A total of 40×200 μL fractions were collected up to a final elution volume of 8 mL. Note that the loading/dead-volume of the PD-10 columns was precisely 2.50 mL which was discarded prior to aliquot collection.

**ADVANCED
SCIENCE NEWS**

www.advancedsciencenews.com

**ADVANCED
NANOBIOMED
RESEARCH**
Open Access

www.advnanobiomedres.com

For quantification of radioactivity, each fraction was measured on a gamma counter (HIDEX Automatic Gamma Counter, Hidex AMG, Turku, Finland) using an energy window between 480 and 558 keV for ^{89}Zr (511 keV emission) and a counting time of 30 s. Appropriate background and decay corrections were applied throughout. PD-10 SEC columns were also used for preparative purification and reformulation of radiolabeled products by collecting a fraction of the eluate corresponding to the high molecular weight protein (>30 kDa fraction eluted in the range between 0.0 to 1.8 mL as indicated for each experiment).

Cell Culture: For cell binding assays, the human ovarian cancer cell line SK-OV-3 (HER2/*neu*-positive, American Type Culture Collection [ATCC-HTB-77], Manassas, VA) was used. Cells were cultured at 37 °C in a humidified 5% CO_2 atmosphere in DMEM/F12 (1:1) (Dulbecco's Modified Eagle Medium, F-12 Nutrient mixture (Ham), ThermoFisher Scientific, Schlieren, Switzerland) medium containing [+]-L-glutamine (2.5 mM), supplemented with fetal bovine serum (FBS, 10% (v/v), ThermoFisher Scientific) and penicillin/streptomycin (P/S, 1% (v/v) of penicillin 10 000 U mL^{-1} and streptomycin 10 mg mL^{-1}). Cells were grown by serial passage and were harvested by using trypsin (0.5%).

The human gastric cancer cell line MKN-45 (Leibniz Institute DSMZ-German collection of Microorganisms and Cell cultures [ACC 409]) was also used. Cells were cultured at 37 °C in a humidified 5% CO_2 atmosphere in RPMI Medium 1640 containing [+]-L-glutamine (2.5 mM), supplemented with FBS (10% (v/v), ThermoFisher Scientific) and penicillin/streptomycin (P/S, 1% (v/v) of penicillin 10 000 U mL^{-1} and streptomycin 10 mg mL^{-1}). Cells were grown by serial passage and were harvested by using trypsin (0.25%).

Animals and Xenograft Models: Animal experiments were conducted in accordance with an experimentation license approved by the Zurich Canton Veterinary Office, Switzerland. Female athymic nude mice (Crl:NU(NCr)-*Foxn1^{nu}*, 20–25 g, 4–8 weeks old) were obtained from Charles River Laboratories Inc. (Freiburg im Breisgau, Germany). Tumors were induced on the right flank by subcutaneous (s.c.) injection of $\approx 7 \times 10^6$ cells suspended in 150 µL of a 1:1 v v^{-1} mixture of PBS and reconstituted basement membrane (Corning Matrigel Basement Membrane Matrix, obtained from VWR International).[37] Animals were randomized to avoid cage effects before administering the radiotracers and commencing the imaging and biodistribution studies.

Small-Animal PET Imaging: PET imaging experiments were conducted on a Genesis G4 PET/X-ray scanner (Sofie Biosciences, Culver City, CA). Radiotracers were administered 200 µL sterile PBS by i.v. tail-vein injection ($t = 0$ h). Then, ≈ 5 min prior to recording PET images, mice were anesthetized by inhalation of 2–3% isoflurane (Baxter Healthcare, Deerfield, IL)/oxygen gas mixture (≈ 5 L min^{-1}) and placed on the scanner bed. PET images were recorded at various time-points between 0 and 90 h postinjection.

Statistical Analysis: Details on the preprocessing (background and decay corrections, data normalization, etc.), sample sizes, and group assignments are given in the appropriate experimental sections and figures. Where appropriate, data were analyzed by the unpaired, two-tailed Student's t test. Differences at the 95% confidence level (P value < 0.05) were considered to be statistically significant. Statistical analysis was performed by using the GraphPad Prism 9 for MAC OS X (version 9.0.0).

Supporting Information

Supporting Information is available from the Wiley Online Library or from the author.

Conflict of Interest

The authors declare no conflict of interest.

Data Availability Statement

Data available on request from the authors.

[1] P. Chakravarty, R. Marches, N. S. Zimmerman, A. D. E. Swafford, P. Bajaj, I. H. Musselman, P. Pantano, R. K. Draper, E. S. Vitetta, *Proc. Natl. Acad. Sci. USA* **2008**, *105*, 8697.

[2] Y. Li, Q. Lu, H. Liu, J. Wang, P. Zhang, H. Liang, L. Jiang, S. Wang, *Adv. Mater.* **2015**, *27*, 6848.

[3] M. R. McDevitt, D. Chattopadhyay, B. J. Kappel, J. S. Jaggi, S. R. Schiffman, C. Antczak, J. T. Njardarson, R. Brentjens, D. A. Scheinberg, *J. Nucl. Med.* **2007**, *48*, 1180.

[4] E. Heister, V. Neves, C. Tîlmaciu, K. Lipert, V. S. Beltrán, H. M. Coley, S. R. P. Silva, J. McFadden, *Carbon N. Y.* **2009**, *47*, 2152.

[5] C. Spinato, A. Perez Ruiz De Garibay, M. Kierkowicz, E. Pach, M. Martincic, R. Klippstein, M. Bourgognon, J. T. W. Wang, C. Ménard-Moyon, K. T. Al-Jamal, B. Ballesteros, G. Tobias, A. Bianco, *Nanoscale* **2016**, *8*, 12626.

[6] S. Srivastava, V. Kumar, K. Arora, C. Singh, M. A. Ali, N. K. Puri, B. D. Malhotra, *RSC Adv.* **2016**, *6*, 56518.

[7] C. Loftus, M. Saeed, D. M. Davis, I. E. Dunlop, *Nano Lett.* **2018**, *18*, 3282.

[8] K. Yang, L. Feng, H. Hong, W. Cai, Z. Liu, *Nat. Protoc.* **2013**, *8*, 2392.

[9] A. Ruggiero, C. H. C. H. Villa, J. P. J. P. Holland, S. R. S. R. Sprinkle, C. May, J. S. Lewis, D. A. D. A. Scheinberg, M. R. M. R. McDevitt, *Int. J. Nanomed.* **2010**, *5*, 783.

[10] S. Shi, C. Xu, K. Yang, S. Goel, H. F. Valdovinos, H. Luo, E. B. Ehlerding, C. G. England, L. Cheng, F. Chen, R. J. Nickles, Z. Liu, W. Cai, *Angew. Chem. Int. Ed.* **2017**, *56*, 2889.

[11] S. Goel, C. G. England, F. Chen, W. Cai, *Adv. Drug Deliv. Rev.* **2017**, *113*, 157.

[12] J. Lamb, E. Fischer, M. Rosillo-Lopez, C. G. Salzmann, J. P. Holland, *Chem. Sci.* **2019**, *10*, 8880.

[13] O. C. Farokhzad, R. Langer, *Adv. Drug Deliv. Rev.* **2006**, *58*, 1456.

[14] D. A. Scheinberg, C. H. Villa, F. E. Escorcia, M. R. McDevitt, *Nat. Rev. Clin. Oncol.* **2010**, *7*, 266.

[15] J. D. Martin, H. Cabral, T. Stylianopoulos, R. K. Jain, *Nat. Rev. Clin. Oncol.* **2020**, *17*, 251.

[16] S. Soares, J. Sousa, A. Pais, C. Vitorino, *Front. Chem.* **2018**, *6*, 1.

[17] J. Shi, P. W. Kantoff, R. Wooster, O. C. Farokhzad, *Nat. Rev. Cancer* **2017**, *17*, 20.

[18] J. Nam, S. Son, K. S. Park, W. Zou, L. D. Shea, J. J. Moon, *Nat. Rev. Mater.* **2019**, *4*, 398.

[19] R. van der Meel, E. Sulheim, Y. Shi, F. Kiessling, W. J. M. Mulder, T. Lammers, *Nat. Nanotechnol.* **2019**, *14*, 1007.

[20] F. Rossella, C. Soldano, V. Bellani, M. Tommasini, *Adv. Mater.* **2012**, *24*, 2453.

[21] S. H. Hu, Y. W. Chen, W. T. Hung, I. W. Chen, S. Y. Chen, *Adv. Mater.* **2012**, *24*, 1748.

[22] H. W. Yang, M. Y. Hua, T. L. Hwang, K. J. Lin, C. Y. Huang, R. Y. Tsai, C. C. M. Ma, P. H. Hsu, S. P. Wey, P. W. Hsu, P. Y. Chen, Y. C. Huang, Y. J. Lu, T. C. Yen, L. Y. Feng, C. W. Lin, H. L. Liu, K. C. Wei, *Adv. Mater.* **2013**, *25*, 3605.

[23] H. Hong, F. Chen, W. Cai, *Mol. Imaging Biol.* **2013**, *15*, 507.

[24] R. K. Jain, T. Stylianopoulos, *Nat. Rev. Clin. Oncol.* **2010**, *7*, 653.

[25] Z. Shi, Y. Zhou, T. Fan, Y. Lin, H. Zhang, L. Mei, *Smart Mater. Med.* **2020**, *1*, 32.

[26] C. Lin, H. Hao, L. Mei, M. Wu, *Smart Mater. Med.* **2020**, *1*, 150.

[27] L. Ding, X. Zhu, Y. Wang, B. Shi, X. Ling, H. Chen, W. Nan, A. Barrett, Z. Guo, W. Tao, J. Wu, X. Shi, *Nano Lett.* **2017**, *17*, 6790.

[28] J. Zhang, D. Chang, Y. Yang, X. Zhang, W. Tao, L. Jiang, X. Liang, H. Tsai, L. Huang, L. Mei, *Nanoscale* **2017**, *9*, 3269.

[29] C. G. Salzmann, V. Nicolosi, M. L. H. Green, *J. Mater. Chem.* **2010**, *20*, 314.

[30] M. Rosillo-lopez,, J. Lee, M. Bella, M. Hart, C. G. Salzmann, *RSC Adv.* **2015**, *5*, 104198.

[31] J. R. Lamb, J. P. Holland, *J. Nucl. Med.* **2018**, *59*, 382.

[32] Y. Zhao, M. Liang, X. Li, K. Fan, J. Xiao, Y. Li, H. Shi, F. Wang, H. S. Choi, D. Cheng, X. Yan, *ACS Nano* **2016**, *10*, 4184.

[33] J. P. Holland, V. Divilov, N. H. Bander, P. M. Smith-Jones, S. M. Larson, J. S. Lewis, *J Nucl. Med.* **2010**, *51*, 1293.

[34] S. Klingler, R. Fay, J. P. Holland, S. Klingler, *J. Nucl. Med.* **2020**, *61*, 1072.

[35] J. P. Holland, E. Caldas-Lopes, V. Divilov, V. A. Longo, T. Taldone, D. Zatorska, G. Chiosis, J. S. Lewis, *PLoS One* **2010**, *5*, e8859.

[36] P. Zanzonico, *J. Nucl. Med.* **2008**, *49*, 1114.

[37] R. Fridman, G. Benton, I. Aranoutova, H. K. Kleinman, R. D. Bonfil, *Nat. Protoc.* **2012**, *7*, 1138.

2100009 (8 of 8)